ELSEVIER

Determining flow type, shear rate and shear stress in magmas from bubble shapes and orientations

A.C. Rust [a,*], Michael Manga [b], K.V. Cashman [a]

[a] *Department of Geological Sciences, 1272 University of Oregon, Eugene, OR 97405-1272, USA*
[b] *Department of Earth and Planetary Science, University of California, Berkeley, CA 94720-4767, USA*

Abstract

We interpret the shear environments that produced bubble textures in obsidian samples using the results of theoretical, numerical and experimental studies on the deformation of bubbles in shear flows. In particular, we use the shapes and orientations of bubbles (vesicles) in obsidian to estimate shear rates and shear stresses, and assess flow type (simple vs. pure shear). This technique can be used to determine shear rates in volcanic conduits, the origin of pyroclastic obsidian, and the emplacement history and dynamics of obsidian flows. A spherical bubble in a viscous fluid subjected to a low Reynolds number, steady flow field deforms until it reaches a steady shape and orientation. Bubble deformation is governed by the competing stresses from shearing that deforms, and surface tension that rerounds. The ratio of these stresses is the capillary number, Ca. Because the relationships among Ca, bubble orientation and shape differ for pure and simple shear, we can distinguish between these flow types using preserved bubble geometries. Furthermore, because Ca is a function of shear rate, we can use relationships between Ca and the magnitude of deformation to calculate shear rates when melt viscosity and surface tension are known. To demonstrate the potential of the technique, we examine three obsidian samples chosen for diversity of origin and texture. Two of the samples have low crystallinities and banding defined by layers of different vesicularity. Bubble geometries in a spatter-fed obsidian flow sample record deformation by pure shear, whereas a juvenile obsidian clast from a pyroclastic fall deposit records predominantly simple shear. A third sample from an obsidian flow has banding marked by variable concentrations of microlites, and shows bubble deformation most consistent with dominantly simple shear and some bubble relaxation. The highest shear rate and shear stress are recorded by the pyroclastic obsidian (shear rate = 0.01 s^{-1}, shear stress = 60 kPa). The spatter-fed obsidian flow sample deformed by pure shear records the lowest shear stress (4.9 kPa). The obsidian flow sample, deformed by simple shear, records the lowest shear rates ($10^{-6.6}$–$10^{-6.9}$ s^{-1}) despite high shear stresses (22–36 kPa) because of the high viscosity of the degassed rhyolite (0.13 wt% water).
© 2002 Elsevier Science B.V. All rights reserved.

Keywords: bubbles; obsidian; simple shear; pure shear; shear rate; shear stress

1. Introduction

Many aspects of volcanic eruptions, including the emplacement of obsidian domes and flow of

* Corresponding author. Fax: +1-541-346-4692.
  E-mail address: arust@darkwing.uoregon.edu
(A.C. Rust).

magma through conduits, lack direct observation and thus require indirect methods to infer flow dynamics. One approach to studying such processes is to analyze the textures of the rocks they produce. The shape, size, orientation and number density of bubbles and crystals can preserve a record of such parameters as magma rheology (Smith, 2000), initial volatile saturation pressure (Toramaru, 1989), ascent velocity (Toramaru, 1989), strain (Manga, 1998), strain rate (Polacci and Papale, 1997), flow direction (e.g. Shelley, 1985), shear sense (Vernon, 1987), effusion rate (Hammer et al., 2000) and cooling rate (Cashman, 1993). In this paper we use a combination of analog experiments and theoretical results to interpret the shape and orientation of bubbles (vesicles) preserved in obsidian. We demonstrate how to use bubble geometries to distinguish between pure and simple shear environments, and to calculate magma shear rates and shear stresses.

Bubbles are nearly ubiquitous in volcanic rocks. Because the preservation of bubble textures is favored by high cooling rates and high melt viscosities, the analysis of bubble shapes for the purposes of determining flow conditions is most easily applied to silicic pyroclasts, lava flows and domes. Here we analyze and interpret bubble geometries in obsidian. The high viscosity of silicic melts results in long relaxation times (e.g. Toramaru, 1988) and the low total bubble content of obsidian minimizes complications from bubble–bubble interactions. Although bubble shapes in basaltic magmas may also be used to study flow dynamics (Polacci and Papale, 1997), the relaxation time is much shorter and bubbles will change shape after emplacement. For example, in pahoehoe, rapid quenching preserves stretched bubbles only within a few millimeters of the flow surface (Self et al., 1998), and internal bubbles relax to a spherical shape prior to solidification (Hon et al., 1994).

Because volcanic glass is transparent and median bubble sizes are small (< 1 mm), we can measure three-dimensional bubble geometries using polished rock slices and a petrographic microscope. We are therefore not limited to interpreting two-dimensional intersections with cut or eroded surfaces, as in studies that use magmatic enclaves as strain markers (Williams and Tobisch, 1994; Tobisch and Williams, 1998; Ventura, 2001). Additionally, in a steady shear flow, the finite surface tension between hydrous gas and silicate melt results in a steady bubble shape once surface tension and viscous stresses are balanced. Thus, unlike microlites (Manga, 1998) or compositionally distinct enclaves (Tobisch and Williams, 1998; Ventura, 2001), bubbles can act as strain-rate markers rather than strain markers. Coward (1980) assumed that bubble aspect ratios indicate magma strain, but this assumption is only true when surface tension can be neglected, which, as we will see, is not an appropriate approximation for small bubbles in volcanic glass.

Bubble deformation is governed by competing stresses from shearing that deforms, and surface tension that minimizes interfacial area. The ratio of these stresses is the capillary number, Ca, which is calculated by

$$\text{Ca} = \frac{aG\mu_s}{\Gamma}, \tag{1}$$

where a is the undeformed bubble radius, G is the shear rate, μ_s is the suspending fluid viscosity, and Γ is the surface tension. As the relationships between Ca and bubble orientation and shape differ for pure and simple shear (e.g. Taylor, 1934; Rallison, 1984; Bentley and Leal, 1986; Stone, 1994), it is possible to distinguish between these flow types using bubble geometries preserved in glassy rocks. Furthermore, because Ca is a function of shear rate, we can use relationships between Ca and bubble deformation, determined from experimental and theoretical studies, to calculate shear rates when melt viscosity and surface tension are known. Similarly, shear stresses ($\sigma = G\mu_s$) can be calculated from bubble geometry data and surface tension.

To demonstrate the application of these techniques to real samples, we examine three obsidian clasts chosen for diversity in origin and texture. Samples include both effusive and pyroclastic obsidian, and clasts with internal banding marked by variable concentrations of bubbles and microlites. We describe how to calculate shear rates and shear stresses from bubble geometries and to distinguish between deformation by pure or simple

shear. These parameters can be used to constrain time scales and physical processes involved in obsidian dome emplacement, flow of silicic magma through volcanic conduits, and the origin of pyroclastic obsidian. The combined analysis of microlite orientation (Manga, 1998; Castro et al., 2002) and bubble geometry thus has the potential to provide a complete picture of flow kinematics and dynamics.

2. Bubble geometry in shear flows

A spherical bubble in a low Reynolds number (Re ≪ 1), steady flow field deforms with a time-dependent shape and orientation until it reaches a steady geometry or breaks into multiple bubbles. With modest deformation, the bubble is spheroidal but pointed ends develop with sufficient deformation. The steady bubble geometry depends on (1) the viscosity ratio, λ, the ratio of the bubble to suspending fluid viscosities, (2) the concentration of surfactants, and (3) the capillary number, Ca (e.g. see review paper by Stone, 1994). Beyond some critical Ca value, Ca_{cr}, which increases with decreasing λ, a bubble cannot sustain a steady shape but deforms continuously and then breaks into smaller bubbles (e.g. Bentley and Leal, 1986).

Based on experimental and theoretical models for Ca_{cr} (Bentley and Leal, 1986; Hinch and Acrivos, 1980; Grace, 1971), vapor bubbles in silicate melts ($10^{-6} < \lambda < 10^{-17}$) are expected to reach a stable (possibly highly deformed) shape rather than break in steady shear flow. We assume that effects of surfactants can be ignored because coalescence textures are abundant in pumice (e.g. Klug and Cashman, 1996; Klug et al., 2002) and there are no known surfactants in magmas. Therefore, provided the concentration of bubbles is sufficiently low that we can neglect the influence of bubble–bubble interaction, a reasonable assumption for the concentrations studied here (Manga et al., 1998), the steady geometry of bubbles will be solely a function of Ca.

To characterize the geometry of a bubble we need to specify its orientation and shape. The flow-induced orientation of a bubble with respect
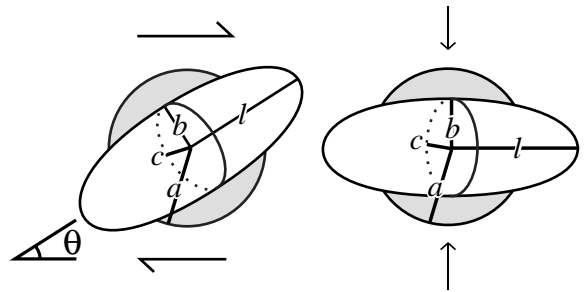

Fig. 1. Schematics of a bubble of radius a, deformed by simple shear (left) and pure shear (right). l, b, and c are semi-principal axes of the deformed bubble ellipsoid, where l is half of the major axis (longest dimension), b is half of the minor axis, and c is half of the intermediate axis perpendicular to both b and l ($b < c < l$). The angle between l and the flow direction is θ.

to the shear flow field is described by the angle θ between the principal axis of the bubble (longest dimension l) and the shear direction, measured in a plane containing both the shear direction and the velocity gradient (Fig. 1). For a single bubble in pure shear flow, elongation is parallel to the shear direction ($\theta = 0$) regardless of the magnitude of bubble deformation. However, in simple shear flow, $\theta = 45°$ for slightly deformed bubbles ($Ca \ll 1$) and decreases toward zero as Ca increases (e.g. Rallison, 1984). We quantify the magnitude of flow-induced bubble deformation using two dimensionless parameters, $D = (l-b)/(l+b)$ and l/a, where l and b are the semi-major and semi-minor axis of the sheared bubble, respectively, and a is the radius of the undeformed bubble (Fig. 1). These parameters are not independent, but D is convenient for small deformations ($Ca \ll 1$) while l/a is useful for $Ca > 1$.

The theoretical relationships for deformation parameters and orientations as a function of Ca for $Re \ll 1$ and $\lambda \ll 1$ are summarized in Table 1. The difference in bubble shapes in pure and simple shear for a given shear rate is dramatic. For example, if $Ca = 10$, a bubble has an aspect ratio (l/b) of about 36 for simple shear and 6.4×10^4 for pure shear. Results of theoretical predictions of shape and orientation for $Ca \ll 1$ agree well with experimental data (Taylor, 1934; Torza et al., 1972; Bentley and Leal, 1986; Guido and Greco,

Table 1

Theoretical equations for bubble orientation and deformation in pure and simple shear with $Re \ll 1$ and $\lambda = 0$

	Pure shear	Simple shear	References
Bubble deformation, $Ca \ll 1$	$D = 2Ca$	$D = Ca$	Taylor, 1932, 1934; Cox, 1969
Bubble deformation, $l/a \gg 1$	$l/a = 16Ca^2$ [a]	$l/a = 3.45Ca^{1/2}$	Hinch and Acrivos, 1980; Buckmaster, 1972; Acrivos and Lo, 1978; Stone, 1994
Bubble orientation, $Ca \ll 1$	$\theta = 0$	$\theta = (\pi/4) - 0.6Ca$	Rallison, 1980; Guido and Greco, 2001
Bubble orientation, $l/a \gg 1$	$\theta = 0$	$\theta = \tan^{-1}(0.359Ca^{-3/4})$	Acrivos and Lo, 1978; Canedo et al., 1993

[a] The constant of proportionality in the bubble deformation equation for $l/a \gg 1$ assumes that $P/G\mu_s = 2$, where P is the pressure in the bubble, which is the only stable solution (Acrivos and Lo, 1978).

2001; Rust and Manga, 2002) and numerical calculations (Rallison, 1981; Pozrikidis, 1993; Kennedy et al., 1994; Uijttewaal and Nijhof, 1995; Loewenberg and Hinch, 1996). Experiments by Rust and Manga (2002) confirm theories derived by Hinch and Acrivos (1980) for bubble ($\lambda \ll 1$) shape and orientation at $l/a \gg 1$, and show that they are applicable to $Ca > 1.0$ and 0.5, respectively. These experimental data span the small and large deformation limits, and allow us to derive empirical equations for $\theta(D)$ and $D(Ca)$ that are good approximations for all bubble deformations ($0 < D < 1$):

$$\theta = \frac{\pi}{2} - D\left(\frac{\pi}{2} + 0.712(D-1)\right) \tag{2}$$

and

$$D = (0.65 + e^{-1.1Ca})\tan^{-1}(Ca). \tag{3}$$

When the shear stress deforming a bubble is removed, the bubble relaxes towards a spherical shape due to surface tension. As its shape relaxes, the bubble orientation remains constant, preserving its shear-induced orientation. Despite their small radius of curvature, the pointed ends of deformed bubbles remain pointed through significant shape relaxation (Rust and Manga, 2002). Therefore, the preservation of pointed ends in obsidian samples does not preclude significant shape relaxation prior to quenching.

The characteristic time scale for bubble relaxation (e.g. Toramaru, 1988), also referred to as the surface tension time scale (e.g. Guido and Greco, 2001), is calculated by:

$$\tau = \frac{a\mu_s}{\Gamma}. \tag{4}$$

For a 100 μm radius bubble and $\Gamma = 0.1$ N/m, if $\mu_s = 100$ Pa s (basalt), $\tau = 0.1$ s, and if $\mu_s = 10^9$ (rhyolite), $\tau = 12$ days. The time for a bubble to reround depends on τ and the initial deformation of the bubble. Bubble relaxation data ($Re \ll 1$, $\lambda \ll 1$) from experiments by Rust and Manga (2002) are fit by:

$$\frac{l-a}{l_i-a} = e^{-0.67t/\tau}, \tag{5}$$

where l_i is the initial (steady) l prior to relaxation, and t is time. Fig. 2 combines Eq. 5 and theories for bubble deformations in steady pure and simple shear flows (Table 1) to show how l/a changes as a function of steady-state Ca (i.e. Ca before shear ceased) as bubbles reround due to surface tension.

3. Methods

Polished thin sections of each sample are made in two or three mutually perpendicular planes. If the glass is clear and the crystallinity low, thin sections thicker than the standard 30 μm increase the number and size of bubbles that can be measured. Ideally, a thin section has an orientation that enables measurements of l, b and θ, which is the plane perpendicular to the shear plane and contains the shear direction and the velocity gradients. If shearing generates flow banding and strains are sufficient to orient the bands parallel
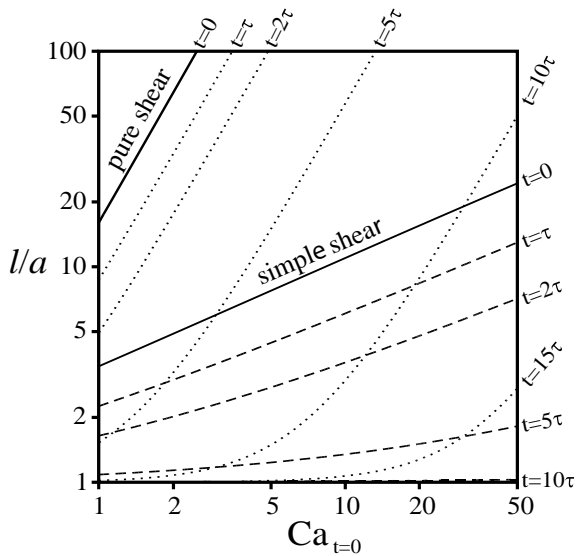
Fig. 2. Dimensionless elongation (l/a) of bubbles deformed in pure (dotted lines) and simple (dashed lines) shear with time as bubble shapes relax due to surface tension once bulk flow ceases. Time is non-dimensionalized by dividing by the characteristic relaxation time (Eq. 4). Solid lines are theoretical high deformation limits for steady flows (Table 1).

to the shear plane, the pertinent plane for measuring θ is perpendicular to flow banding and parallel to flow lineation, marked by alignment of high aspect ratio bubbles or crystals.

Bubbles are photographed with a digital camera attached to a petrographic microscope. The fastest, most consistent method to determine bubble dimensions is to print photomicrographs and measure lengths with a digital micrometer. Bubble orientations are determined using NIH image software. The principal axes of the bubbles are manually designated, and for the samples with only one or two bubbles in focus per image, lines marking bubble orientations from multiple photomicrographs are combined into a single bitmap. When the orientation of slightly deformed bubbles is difficult to judge, photomicrographs are directly imported into NIH image without marking principal axes.

4. Case studies

Our aim is to use the geometry of bubbles in glassy volcanic rocks to estimate shear rates and make qualitative assessments of flow type (e.g. simple vs. pure shear). To demonstrate the potential of the technique, we examine three obsidian samples. The Mayor Island (MI) sample is from a spatter-fed obsidian flow, the Rock Mesa (RM) sample is obsidian from a pyroclastic fall deposit, and the Big Glass Mountain (BGM) sample is from an effusive obsidian flow. With this sample set we have both effusive (MI, BGM) and pyroclastic (RM) obsidian, banding marked by variable concentrations of both bubbles (MI and RM) and microlites (BGM), and anticipated flow regimes that are both dominantly pure shear (MI) and simple shear (RM and BGM). The vesicularities and crystallinities of bands in the three samples are listed in Table 2. Table 3 summarizes the results of the bubble geometry analyses.

4.1. Mayor Island (MI)

The Mayor Island sample (MI) is from the 8 ka, fountain-fed, pantelleritic lava flow, Mayor Island, New Zealand. It was collected from the upper obsidian layer (Stevenson et al., 1993) at Taratimi Bay. Based on large scale flow morphology and textures of relict clasts in the basal obsidian layer, Stevenson et al. (1993) infer that spatter from a lava fountain accumulated near the caldera rim, homogenized and remobilized as a lava flow. Although fire fountains are common in basalt eruptions, they require relatively low magma viscosities, and thus are generally not possible in rhyolite eruptions. However, strongly peralkaline rhyolite such as the 8 ka Mayor Island flow has sufficiently low viscosity that rapidly accumulated pumice can compact and remobilize.

Fig. 3 shows photomicrographs of the MI sample taken in two orientations, both of which are perpendicular to banding defined by layers of variable bubble concentrations. The main photomicrograph (Fig. 3a) is parallel to the bubble elongation direction and is suitably oriented for measuring l, b, and θ. The inset (Fig. 3b) shows bubbles in a plane oriented perpendicular to the bubble lineation. A photograph of bubbles in a shear plane (parallel to banding; perpendicular to both Fig. 3a,b) is published in Manga et al. (1998).

Table 2
Vesicularity and crystallinity data

Sample	Band #	Vesicularity (%)	Crystallinity (%)
Mayor Island	1	12	$\ll 1$
	2	11	$\ll 1$
	3	18	$\ll 1$
	4	10	$\ll 1$
	5[a]	25	$\ll 1$
Rock Mesa	1	0.4	$\ll 1$
	2	$\ll 1$	$\ll 1$
	3	$\ll 1$	$\ll 1$
	4	$\ll 1$	$\ll 1$
	5	3.0	$\ll 1$
	6	1.1	$\ll 1$
	7	1.6	$\ll 1$
	8	0.8	$\ll 1$
Big Glass Mountain	1	$\ll 1$	0.9
	2	$\ll 1$	1.6
	3	$\ll 1$	0.6
	4	$\ll 1$	1.4

[a] Bubbles in Mayor Island band 5 were only measured in cross-section (perpendicular to flow direction).

We can make useful, qualitative observations from the thin sections without measuring any bubbles. It is clear from Fig. 3a that the degree of deformation is a function of bubble size. While the smallest bubbles are nearly spherical and slightly larger bubbles are spheroidal, the largest bubbles are elongate with pointed ends. Unlike shape, bubble orientation is not a function of size. Bubbles are elongate parallel to both banding and to the average orientation of sparse microlites. This alignment of prolate bubbles (Fig. 3a) is consistent with deformation in a flow field dominated by two-dimensional pure shear (e.g. Rallison, 1984).

Qualitative observations are confirmed and quantified with data from 333 bubbles. Measure-ments of l, b and θ were made from bubbles within the area of Fig. 3a, as well as from areas of similar size in two other bands of the same thin section. D is calculated from measurements of l and b. To calculate the non-deformed bubble radius for determining l/a, we examine the cross-sectional shapes of bubbles. Perpendicular to elongations, bubbles are elliptical (Figs. 3b and 4) with aspect ratios independent of band vesicularity and only slightly dependent on bubble size. Data from two bands with vesicularities of $\phi = 0.10$ and 0.25, respectively (Fig. 4), are well described by:

$$c = 0.0151b^2 + 1.37b, \text{ for } b \text{ and } c \text{ in } \mu m, \qquad (6)$$

where c is the semi-principal axis of the elliptical

Table 3
Flow type and Ca/a determined from bubble geometries, and physical properties of fluids (μ_s and Γ) used to calculate shear rate (G) and shear stress (σ)

Sample	Flow type	log Ca/a (m^{-1})	log μ_s (Pa s)	Γ (N/m)	log G (s^{-1})	σ (kPa)
MI	pure	4.2	8.87	0.3	−5.2	4.9
RM	mostly simple	5.2–5.5[a]	6.7	0.3	−2	60
BGM bands 2, 4	mostly simple,	5.1	11.2	0.3	−6.6	36
BGM bands 1, 3	some bubble relaxation	4.9	11.2	0.3	−6.9	22

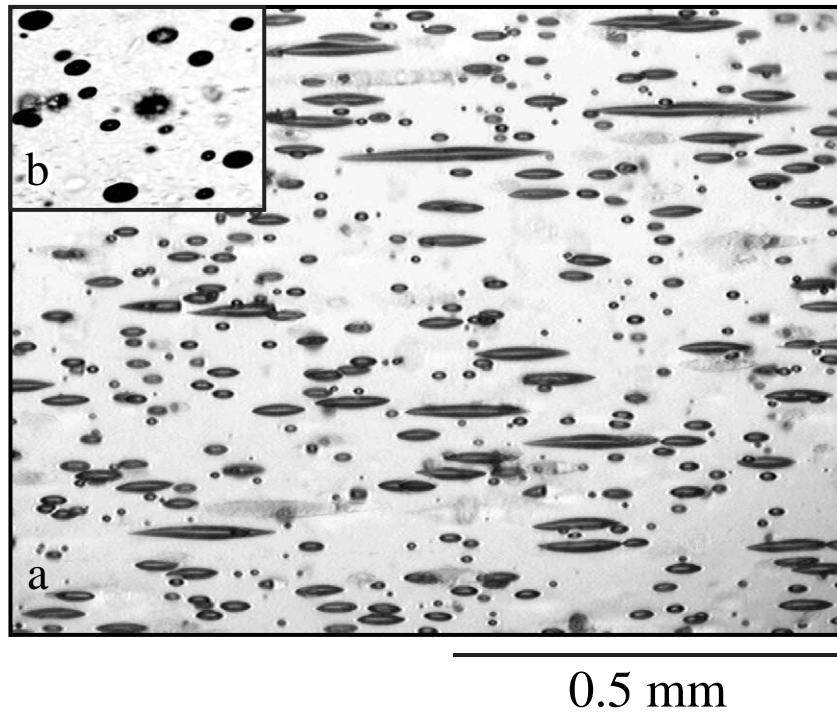[a] log Ca/a = 5.3 used to calculate G and σ.

Fig. 3. Photomicrographs of the Mayor Island sample perpendicular to flow banding, (a) parallel to the bubble elongation lineation, and (b) perpendicular to the bubble lineation.

section of the bubble perpendicular to the elongation of the bubble (Fig. 1). We assume the bubble volume is constant throughout deformation, approximate the bubble as ellipsoidal, and calculate bubble radius from:

$$a = (lbc)^{1/3}. \tag{7}$$

Additional data are obtained from a thin section parallel to the shear plane (parallel to banding). For this thin section l and c are measured directly and b is calculated from data in Fig. 4. Most of the bubbles measured are from an area 1 mm by 0.8 mm (figure 1 of Manga et al., 1998). To extend the range of bubble sizes, we include data from the 18 largest bubbles in the thin section that are approximately symmetrical and have both ends within the glass.

To determine how the deformation parameters D and l/a vary with Ca, we plot both as a function of a, which is proportional to Ca (Eq. 1) for constant G, Γ and μ_s (Fig. 5). In Fig. 5a, a straight line fit to the data for $D < 0.5$ and $a < 15$ μm is

$D = 0.0326a$. Based on the alignment of bubbles parallel to banding and average microlite orientations, we assume that the flow is pure shear and capillary numbers can be calculated (Table 1) from $Ca = D/2 = 0.0163a$, where a is in μm. This relationship was used to determine the upper horizontal axes in Fig. 5b. Similar fits to subsets of data from different bands (Table 2) give relationships ranging from $Ca = 0.0140a$ (band 4) to $Ca = 0.0185a$ (band 2). With increasing a, the data approach $l/a \propto a^2 \propto Ca^2$, which is consistent with pure shear flow (Fig. 5b). For $l/a > 5$, the data match the theoretical $l/a \gg 1$ upper limit (solid line in Fig. 5b) remarkably well, although there were only sufficiently large bubbles in band 1 to define this trend.

Rearranging Eq. 1, we see that shear rate (G) and shear stress ($\sigma = \mu_s G$) are functions of Ca/a:

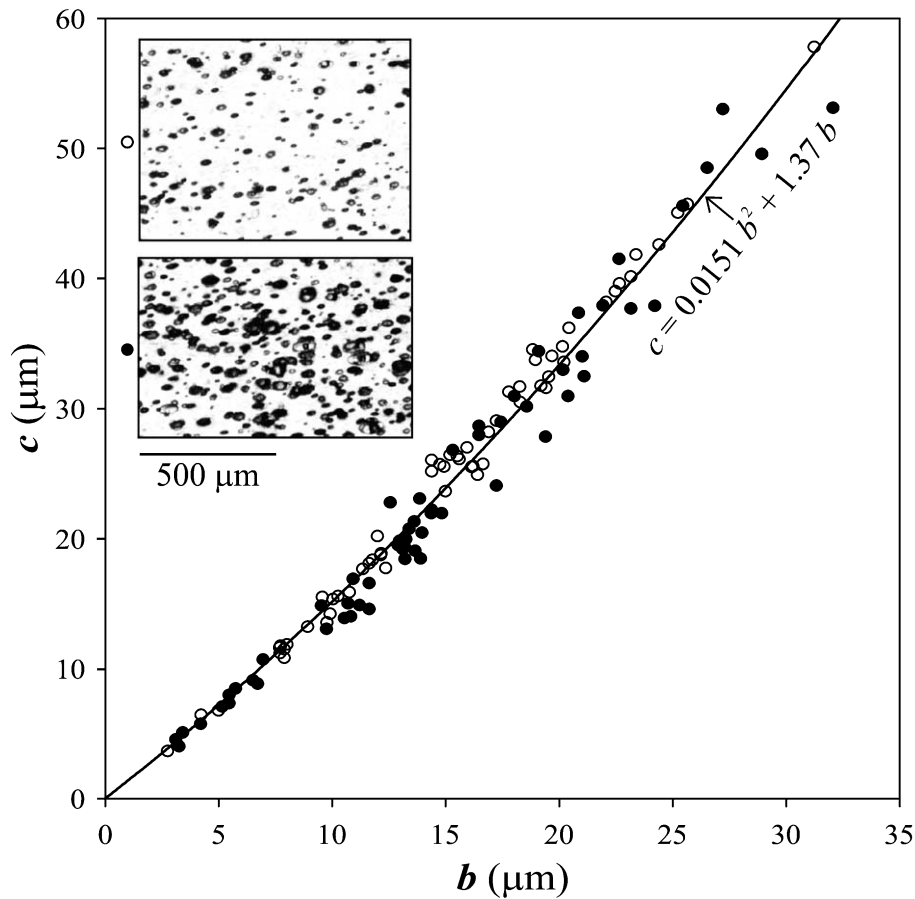$$G = \frac{Ca}{a} \frac{\Gamma}{\mu_s} \tag{8}$$

and

Fig. 4. Plot of dimensions of the elliptical cross-sections of bubbles in two bands of the Mayor Island sample (bands 4 and 5 of Table 2). The semi-major axis of the cross-sectional ellipse is c, and the semi-minor axis of the ellipse is b (see Fig. 1). Open symbols are for band 4, filled symbols are for band 5. The photomicrographs of portions of these bands were taken with transmitted light.

$$\sigma = \frac{\mathrm{Ca}}{a}\Gamma. \qquad (9)$$

Therefore we can calculate G and σ with estimates of melt viscosity and bubble–melt surface tension. Stevenson et al. (1995) measured the viscosity of obsidian from the 8 ka Mayor Island lava flow using the parallel-plate method of Bagdassarov and Dingwell (1992). We use the viscosity at 692°C ($10^{8.87}$ Pa s), which is their highest temperature measurement (the sample vesiculated at 710°C, 1 atm). For surface tension we use $\Gamma = 0.3$ N/m based on recent experiments by Bagdassarov et al. (2000) on Armenian rhyolite extrapolated to 700°C. With these parameters, and $\mathrm{Ca}/a = 1.63 \times 10^4$ m^{-1}, the shear rate and shear

stresses calculated for the Mayor Island obsidian sample are 6.6×10^{-6} s^{-1} and 4.9 kPa, respectively (Table 3).

4.2. Rock Mesa (RM)

The second sample is an obsidian clast from a 2200 yr BP pyroclastic fall deposit from Rock Mesa (RM) on the southwest flank of South Sister Volcano, Oregon, USA (mapped by Scott, 1987). Obsidian is a common component of pyroclastic deposits that are associated with obsidian flows (e.g. Newman et al., 1988; Rodgers, 1996; Gardner et al., 1998). Obsidian is found throughout the Rock Mesa pyroclastic fall deposit along
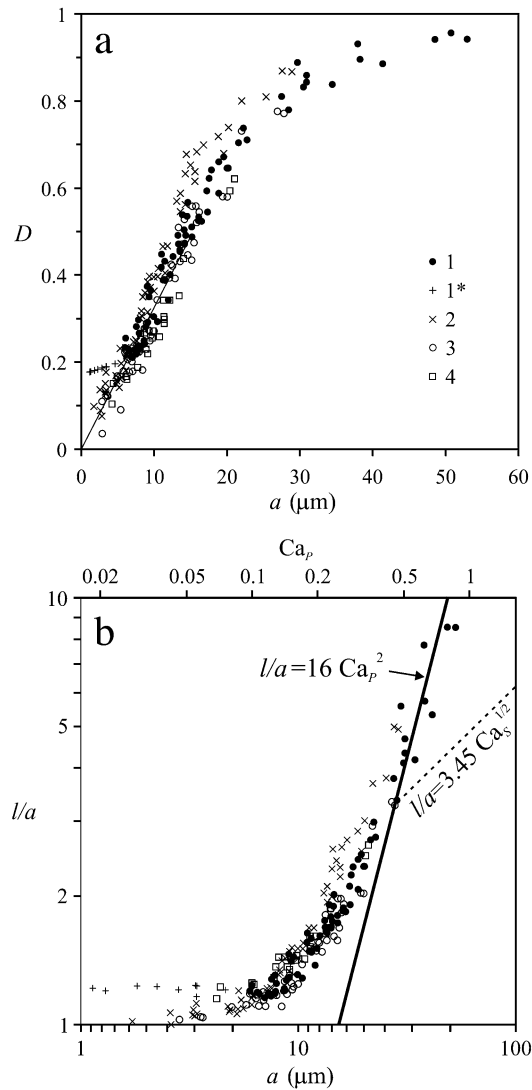
Fig. 5. Plot of Mayor Island bubble deformation data: (a) D vs. Ca and (b) l/a vs. Ca. The upper x-axis in panel b is capillary number calculated from the D/a fit in panel a, assuming pure shear ($Ca_p = D/2$). The solid line in panel b is the theoretical high deformation relationship for pure shear of Acrivos and Lo (1978); the dotted line is the high deformation prediction by Hinch and Acrivos (1980) for simple shear with capillary numbers calculated from the D/a fit of panel a and assuming simple shear ($Ca_s = D$). The numbers in the legend correspond to the MI bands in Table 2. The data for bands 2–4 are from a thin section parallel to the flow direction and perpendicular to banding (shear plane). The data from band 1 are from a thin section that is parallel to the banding and thus involve measurements of l and c. The plus symbols (+) are for a subset of the data in band 1 ($a < 9$ μm) for which the longest dimension of the bubbles is perpendicular to the elongation of larger bubbles in the thin section. For these bubbles we let l be half of the length of the bubble in the direction of the elongation of larger bubbles. Thus for these bubbles we let $l < c$.

with white pumice, gray (microlite-rich) pumice, and non-juvenile lithics. The clast we examine was collected at site 2 of Rodgers (1996), 2300 m south of the Rock Mesa vent, 1 m from the base of the deposit, which is 2.1 m thick at this location. At this stratigraphic level, the juvenile component of the 4–8 mm size fraction of the tephra is 49 wt% white pumice, 35 wt% obsidian,
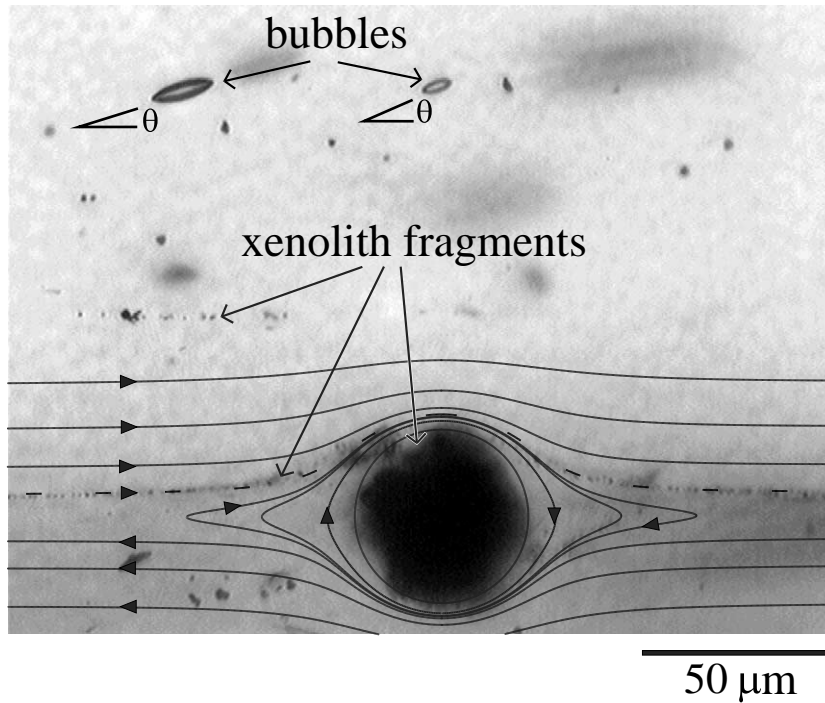
Fig. 6. Photomicrograph of the Rock Mesa sample (location indicated in Fig. 7). Picture is perpendicular to banding, with lower and upper edges parallel to banding. A flowline marked by tiny xenolith pieces is deflected around a larger xenolith fragment. This flowline closely resembles a theoretical streamline (dashed line) for simple shear around a 45 μm sphere (Manga, 1998). Bubbles are oriented at an angle to the banding (and the straight portions of the streamline) which is consistent with dominantly simple shear flow with the top of the picture moving from left to right with respect to the bottom.

and 16 wt% gray pumice (Rodgers, 1996). The clast is vitreous (crystallinity, $\phi_c \ll 0.01$) with banding defined by variations in vesicularity.

FT infrared spectroscopy analyses of glass in different bands of the sample range from 0.9 to 1.2 wt% total H_2O and 2–11 ppm molecular CO_2. These water contents correspond to a depth of about 450 m (assuming magmastatic pressure), confirming that the obsidian fragmented in the conduit and is not the result of destruction of a pre-existing obsidian dome. We calculate a melt viscosity (μ_s) of $10^{6.7}$ Pa s using the hydrous granitic melt viscosity model of Hess and Dingwell (1996), assuming a temperature of 850°C and 1.1 wt% water (average of six FTIR analyses). The average cooling rate calculated from H_2O_m and OH data (Zhang et al., 2000) is 22°C/s. Because such rapid cooling leads to rapid viscosity

increase, bubble shape relaxation after fragmentation is not an issue.

Preliminary examination of thin sections of RM obsidian suggests that, in contrast to the MI flow sample, deformation was dominated by simple shear. First, the rare high aspect ratio microlites are, on average, parallel to banding (defined primarily by vesicularity) but the bubbles are oriented at an angle to banding. Furthermore, θ is a decreasing function of bubble size. Finally, a streamline marked by a thin band of fine xenolith material around a larger xenolith fragment (Fig. 6) is consistent with simple shear around a freely rotating sphere (Manga, 1998).

Bubble dimensions (l and b) and orientations (θ) were measured in eight bands marked in Fig. 7. The vesicularity and crystallinity of these bands are listed in Table 2. Unfortunately, these mea-
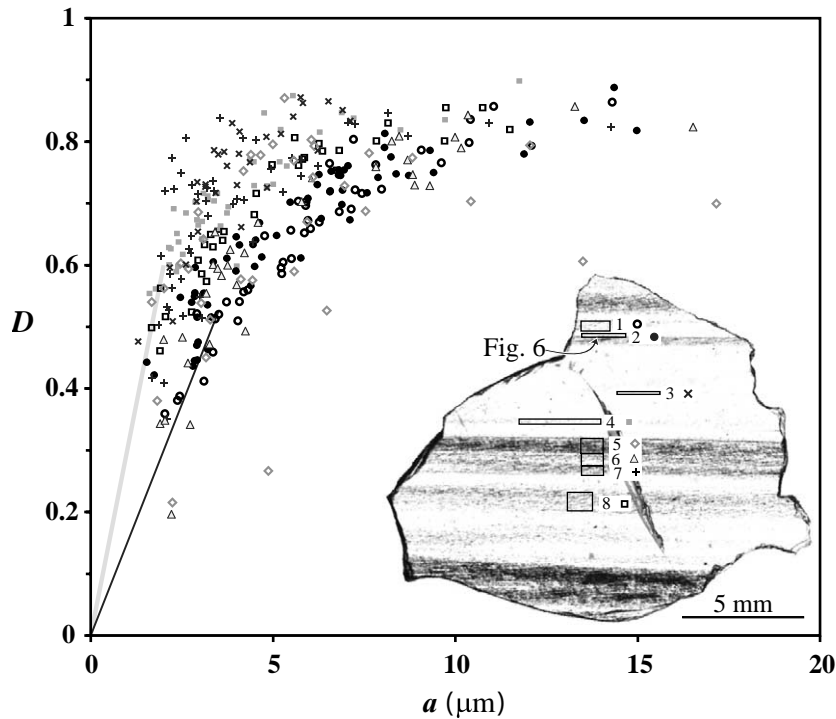
Fig. 7. Plot of bubble deformation parameter $D = (l-b)/(l+b)$ vs. bubble radius for the Rock Mesa sample. The thick gray line is $D/a = 3.0 \times 10^5$ m^{-1}, the thin black line is $D/a = 1.5 \times 10^5$. The inset is a photograph of the Rock Mesa thin section parallel to flow direction. The greater the porosity, the darker the band. Boxes on the photograph indicate regions from which bubble geometry data were collected. The numbers and symbols to the right of these boxes correspond to the band numbers in Table 2 and symbols used in Figs. 8 and 9.

surements provide few data for bubbles with minor deformation ($D < 0.5$) that are most useful for calculating Ca and G (cf. Eq. 8). We make estimates of Ca/a by drawing bracketing lines from the origin to the cluster of data near $D = 0.5$ (Fig. 7). Assuming simple shear and thus $D = $ Ca for small D (Taylor, 1934), we estimate $1.5 \times 10^5 \leq$ Ca/$a \leq 3.0 \times 10^5$ m^{-1}. Using $\mu_s = 10^{6.7}$, $\Gamma = 0.3$ N/m and Ca/$a = 2 \times 10^5$ m^{-1}, we calculate $G = 1 \times 10^{-2}$ s^{-1}, $\sigma = 60$ kPa. The calculated shear rate for the Rock Mesa pyroclast is three orders of magnitude greater than for the Mayor Island lava flow sample (Table 3).

In simple shear, the orientation of bubbles (θ) should be related to D (Table 1; Eq. 2) which in turn depends on Ca (Table 1; Eq. 3). For all bands, $\theta(D)$ is less than expected for simple shear (Fig. 8). Deviations from experimental (Rust and Manga, 2002) and theoretical (Canedo et al.,

1993) results increase with decreasing vesicularity. If the variation in θ with vesicularity were the result of bubble–bubble interactions, we would expect the data from the lowest vesicularity bands to most closely resemble analog experiments on single bubbles. Simulations of concentrated emulsions by Loewenberg and Hinch (1996) also indicate that bubble–bubble interactions should reduce θ. Our data thus require an alternative explanation.

In the MI sample, we saw that pure shear produced bubbles with $\theta = 0$ (Fig. 3). Therefore our RM bubble orientation data could be explained by a pure shear component to the deformation that increased with decreasing vesicularity. This notion is corroborated by trends in the l/a versus a plots (Fig. 9). Band 8 ($\phi = 0.008$; Fig. 9c) bubbles best fit the theoretical high l/a limit of Hinch and Acrivos (1980) (Table 1) and experimental
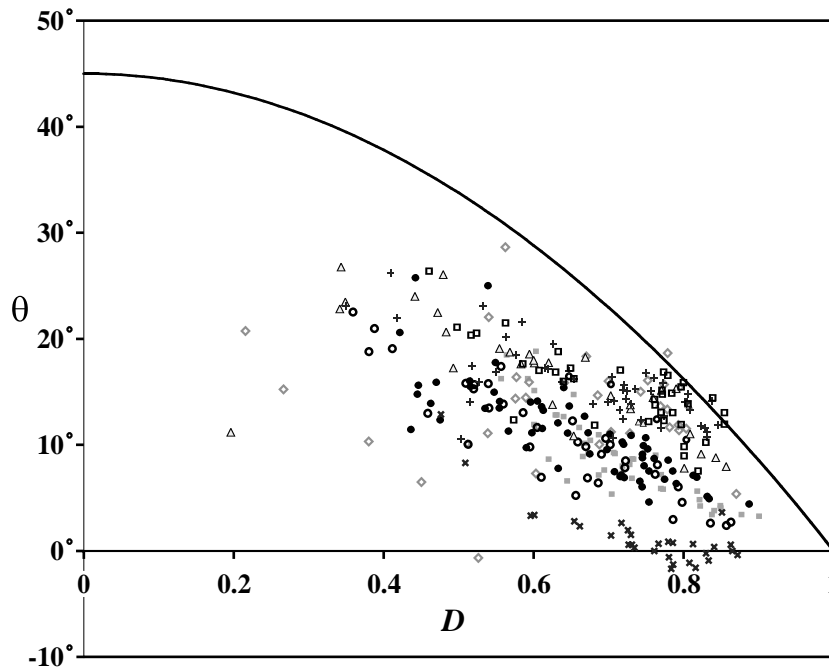
Fig. 8. Plot of orientation of bubbles relative to banding vs. bubble deformation parameter *D*. Symbols are the same as in Fig. 7. The curve is Eq. 2, which is a fit to experimental data (Rust and Manga, 2002) on bubble orientations in simple shear flow. In pure shear $\theta = 0$.

data (Rust and Manga, 2002) for simple shear. Bubbles in lower vesicularity bands (bands 1–4; $\phi = 0.004$, $\ll 0.01$, $\ll 0.01$, and $\ll 0.01$) as well as the slightly more vesicular band 6 ($\phi = 0.011$) all show deviations from simple shear towards the expected higher slope for pure shear (Fig. 9a,b), with the greatest deviation from the lowest vesicularity band (band 3). It is difficult to define the relative contributions of pure and simple shear, as the relationships among orientation, deformation and bubble size are not linear, and thus solutions to the simple and pure shear cases cannot be superposed (Stone, 1994). Slight variations in flow type within the sample could also account for much of the observed range in *D/a* (Fig. 7).

Deformation data from the two most vesicular bands (5 and 7; $\phi = 0.030$, 0.016) have the greatest scatter (Fig. 9d). Our only explanation is that bubbles cause local perturbations in shear rate and flow direction, thus affecting the shape and orientations of neighboring bubbles. Despite much greater vesicularities ($0.09 < \phi < 0.15$) in

the four MI bands, the MI data show much less scatter (Figs. 4 and 5). The MI sample was deformed by pure shear whereas the RM sample by dominantly simple shear. Because all bubbles are parallel in pure shear, bubbles may have less effect on neighboring bubbles.

4.3. Big Glass Mountain (BGM)

The third sample is from Big Glass Mountain (BGM), a rhyolite obsidian dome at Medicine Lake, California, USA. The sample was collected at the flow front and exhibits banding defined by variable concentrations of clinopyroxene microlites (determined by SEM). Bubble geometries were measured in four bands (Fig. 10). Because of very low vesicularity ($\phi \ll 0.01$), within each band, bubble geometries were measured over areas as large as 90 mm^2 (using two thin sections).

The flow direction, marked by microlite alignment, is clear. Fractured or sawn surfaces approximately perpendicular to the microlite lineation
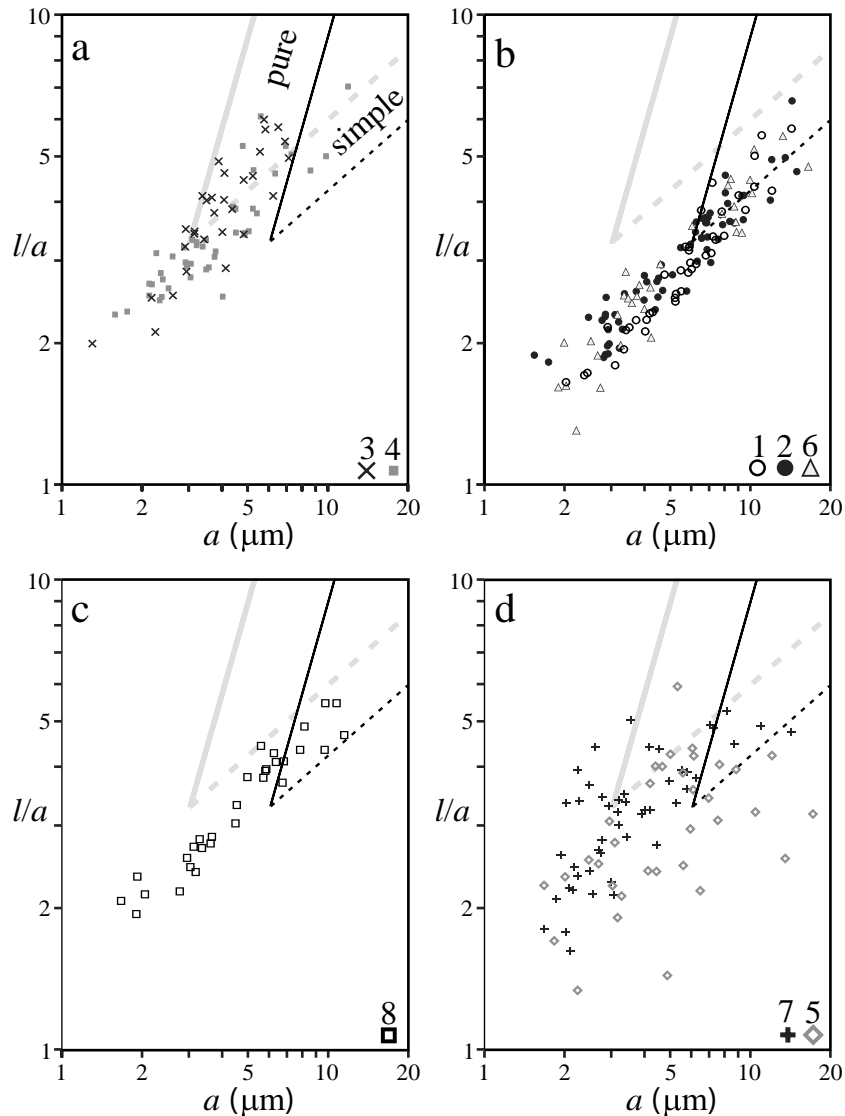
Fig. 9. Plots of dimensionless bubble elongation (l/a) vs. bubble radius (a) for bubbles in eight bands of the Rock Mesa sample. Symbols are the same as in Fig. 7. Solid and dashed lines are theoretical relationships for high deformation in pure shear and simple shear, respectively (Table 1). As in Fig. 7, thick gray lines (solid and dashed) are based on $D/a = 3.0 \times 10^5$ m^{-1}, and the thin black lines are based on $D/a = 1.5 \times 10^5$ m^{-1}.

appear black in hand sample with banding faint or not visible. A thin section in this orientation shows that bands are not parallel and some band thicknesses are variable (Fig. 10a). However, if cut in a particular orientation parallel to flow direction (Fig. 10b; explained further below), the bands appear parallel. In simple shear flow, any pre-existing folds or heterogeneities are smeared

in the flow direction but are preserved in the plane perpendicular to the flow direction. The banding geometry could also be produced by two-dimensional pure shear which flattens heterogeneities parallel to the principal stress (perpendicular to the flow direction) and stretches heterogeneities parallel to the flow direction. Therefore the bands in this sample do not represent shear planes and
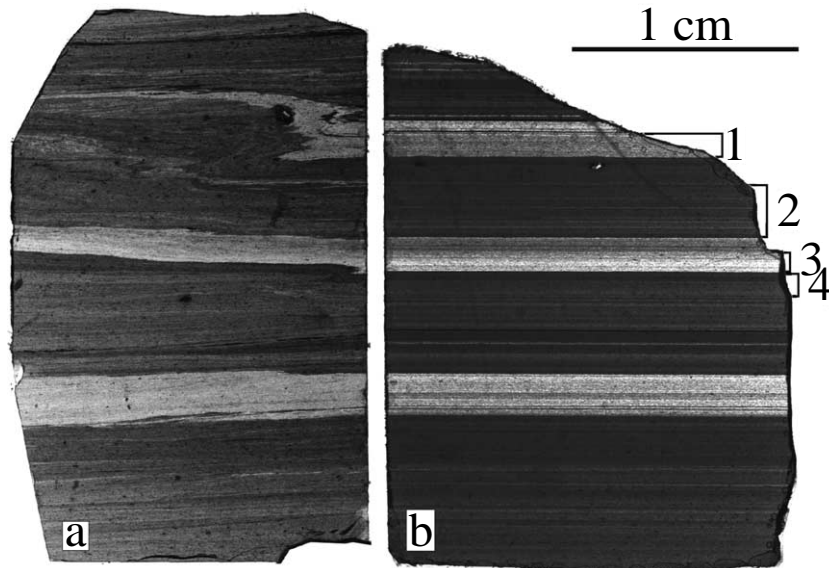
Fig. 10. Thin sections of the Big Glass Mountain sample: (a) perpendicular to flow direction, (b) parallel to flow direction. Numbers mark the four bands from which bubble data were obtained (Table 2). The darkness of bands correlates with microlite content.

their geometry is consistent with simple shear or two-dimensional pure shear.

We made two thin sections for l, b, and θ measurements. The optimal orientation for these measurements is perpendicular to the shear plane and parallel to the flow direction. The shear plane orientation is not known, so the thin sections were made approximately perpendicular to the average orientation of the bands in the thin section perpendicular to the flow direction (Fig. 10). Both contain the mineral lineation, but the thin section orientations differ by 5°. Data from the two thin sections are not significantly different. In these thin sections, the bands are of constant thickness and parallel to the microlite lineation (Fig. 10b), as expected for a plane containing the velocity gradient and flow direction.

Deformation parameters and orientations of bubbles from the four bands marked in Fig. 10b are plotted in Figs. 11 and 12. Bubble radii were calculated by Eq. 7 using $c = 1.23b$, based on aspect ratios of bubbles perpendicular to the flow direction. We group the bubble geometry data based on band crystallinity, with bands 1 and 3 having relatively low crystallinity ($\phi_c = 0.009$ and

0.006, respectively) and bands 2 and 4 having relatively high (but low in absolute terms) crystallinity ($\phi_c = 0.016$ and 0.014, respectively). Within each band there is banding on a smaller scale and the ϕ_c values (Table 2) are averages for the mm-scale bands.

Linear best fits to small deformation data (Fig. 11a) give $D/a = 1.2 \times 10^5$ m^{-1} and $D/a = 7.3 \times 10^4$ m^{-1} for the higher and lower crystallinity bands, respectively. The most deformed bubbles in all bands satisfy $l/a \propto a^{1/2}$, which is consistent with simple shear flow (Fig. 11b), although the bubbles in the low ϕ_c bands are less deformed than predicted for simple shear. For the purpose of determining shear rates, we assume simple shear flow for all bubbles in this sample and therefore use $Ca = D$ to calculate Ca from low D data. For $\Gamma = 0.3$ N/m and $\mu_s = 10^{11.2}$ Pa s (the viscosity of Little Glass Mountain melt at 856°C (Webb and Dingwell, 1990)), $Ca/a = 1.2 \times 10^5$ m^{-1} and $Ca/a = 7.3 \times 10^4$ m^{-1} correspond to $\sigma = 36$ kPa, $G = 2.3 \times 10^{-7}$ s^{-1} and $\sigma = 22$ kPa, $G = 1.4 \times 10^{-7}$ s^{-1}, respectively.

In the above calculations Γ, μ_s, and shear type are assumed constant and therefore the variations
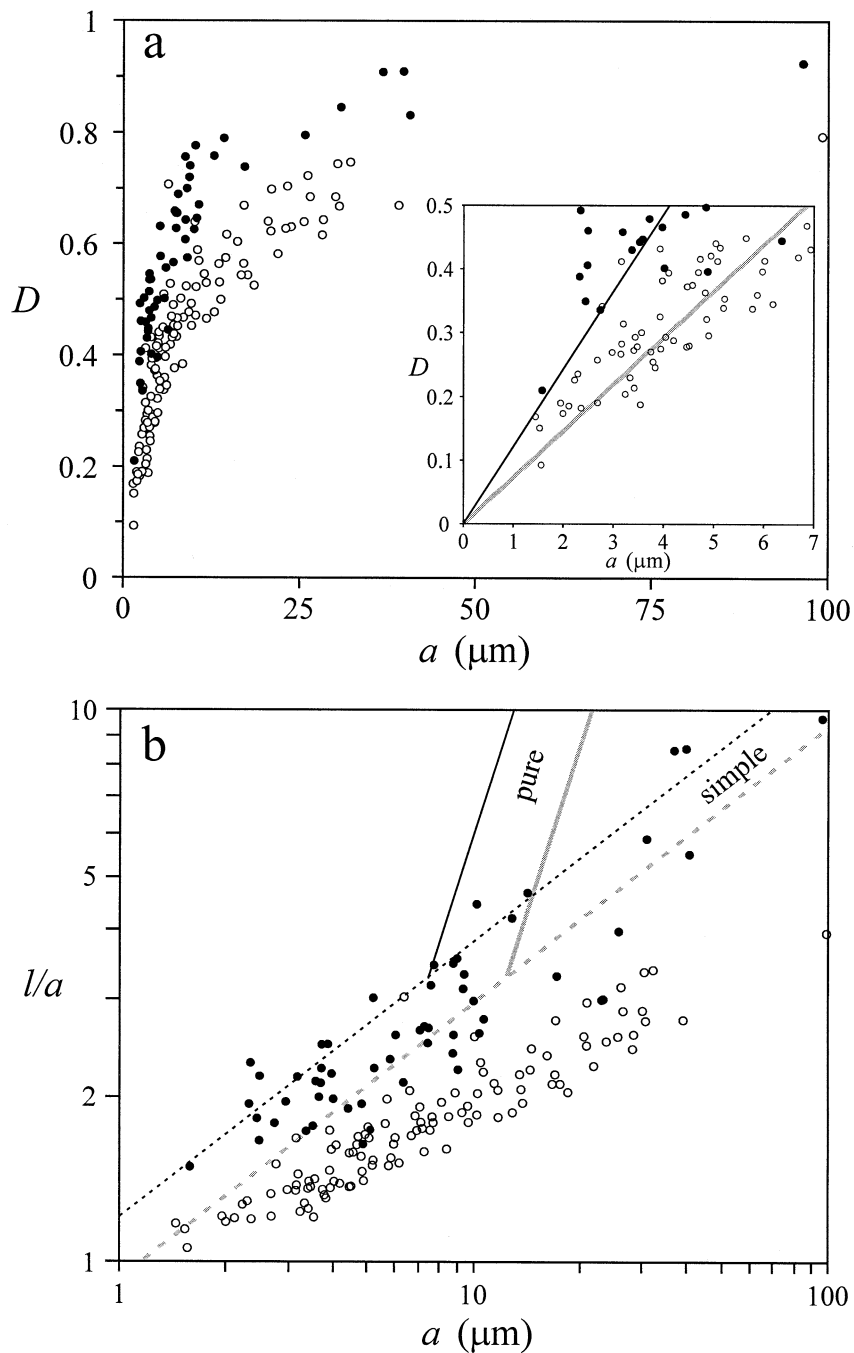
Fig. 11. Deformation of bubbles in the Big Glass Mountain sample as a function of bubble radius. Black filled circles are from the relatively higher crystallinity bands 2 and 4, and open circles are data from bands 1 and 3 (Fig. 10; Table 2). (a) Plot of D vs. a. The thick gray line in the inset (fit to open circles) is $D/a = 7.3 \times 10^4$ m^{-1}; the thin black line (fit to filled circles) is $D/a = 1.2 \times 10^5$ m^{-1}. (b) Plot of l/a vs. a. Solid and dashed lines are theoretical relationships for high deformation in pure shear and simple shear, respectively (Table 1). Thick gray lines (solid and dashed) and thin black lines are based on D/a relationships marked in the inset of panel a.

in D/a ratios are attributed to shear localization. Other possible contributors to the greater D/a (and thus greater apparent G) in the high ϕ_c bands are smaller Γ, greater μ_s, and a greater component of pure shear in these bands. It is reasonable to assume constant Γ because surface tension is not sensitive to small differences in composition (Bagdassarov et al., 2000). Melt viscosity is very sensitive to water content for low water concentrations (Hess and Dingwell, 1996; Schulze et al., 1996); however, FT infrared spectroscopy analyses of total water content in all four bands are indistinguishable (0.131–0.132 wt%). Given that the melts have identical water contents and crystals increase the bulk viscosity of magmas (e.g. Pinkerton and Norton, 1995; Ryerson et al., 1988; Bagdassarov et al., 1994; Lejeune and Richet, 1995), it seems unlikely that the 1.6 times greater D/a for the high ϕ_c bands over the low ϕ_c bands reflects greater shear rates in the former. However, it is possible that higher shear rates promote crystal nucleation (Kouchi et al., 1986). If variations in D/a are not due to G differences, there must be variations in shear type. A component of pure shear in the high ϕ_c bands is plausible. As discussed further below, the high deformation bubble data and bubble orientation data are most simply explained by there being a component of pure shear in the high ϕ_c bands and all bubbles undergoing some shape relaxation.

Deformation data for bubbles in the high ϕ_c bands lie just below the theoretical limit for simple shear for $l/a \gg 1$ (Table 1; Fig. 11b) in accord with experimental results of bubble shapes in simple shear (Canedo et al., 1993; Rust and Manga, 2002). However, data for the low ϕ_c bands do not follow predicted trends for either pure or simple shear. Our experimental results (Rust and Manga, 2002) indicate that the high deformation limit ($l/a = 3.45\text{Ca}^{1/2}$) for simple shear predicted by Hinch and Acrivos (1980) is a good approximation for Ca > 1, which corresponds to $a > 13.7$ μm for bubbles in the low ϕ_c bands. Bubbles in these bands with Ca > 1 satisfy $l/a \propto a^{1/2}$, but the constant of proportionality is considerably less than predicted. The simplest explanation is shape relaxation after the cessation or reduction of shear stress. Comparison of these data with Fig. 2 sug-
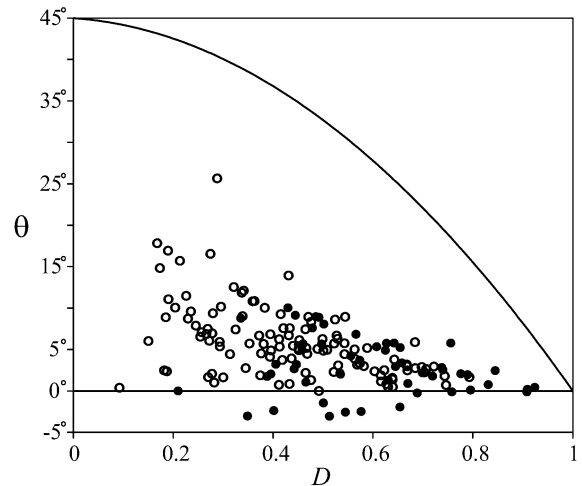

Fig. 12. Plot of orientation of bubbles relative to banding vs. bubble deformation parameter D. Symbols are the same as in Fig. 11. The curve is Eq. 2, which is a fit to experimental data (Rust and Manga, 2002) on bubble orientations in simple shear flow. In pure shear $\theta = 0$.

gests a relaxation time of about one characteristic relaxation time (Eq. 4) if flow was entirely simple shear. An alternative explanation is that equilibrium bubble shapes were never achieved. The time scale for a bubble to reach a steady shape in steady shear flow is of the same order as for shape relaxation (Hu and Lips, 2001). However, bubble orientation data are not consistent with the hypothesis that bubbles never reached steady shapes.

Bubble orientations are not altered by bubble relaxation and thus preserve the orientation of bubbles prior to relaxation (Rust and Manga, 2002). Therefore, if bubble relaxation is a factor then bubbles should be oriented at smaller angles to the flow direction than predicted (given their shape) for simple shear. This is true for bubbles in all four bands analyzed (Fig. 12). Lower θ than expected for a given bubble deformation could also be caused by a component of pure shear, by bubble expansion, or by particle–particle interactions, but not by lack of sufficient strain for bubbles to reach their steady shapes. Therefore, bubble orientation data are consistent with bubble relaxation and not with transient bubble shapes. Given that bubbles in the lower crystallinity bands seem to have relaxed and bubbles in all

bands have much smaller θ than predicted for simple shear, it is likely that the bubbles in the higher crystallinity bands have also relaxed. In these bands, the preserved bubble shapes as a function of size approach predictions of high deformation theory for simple shear. To have relaxed to this geometry requires a small component of pure shear that creates higher deformations for the same Ca. This could account for the differences in D/a for the bands (Fig. 11a) without invoking differences in melt viscosity or shear rate.

5. Errors in determining G and σ

Potential sources of error in calculations of shear rate and shear stresses from bubble geometries include estimates of melt viscosity, surface tension, and flow type as well as the effects of shape relaxation, bubble growth, transient bubble shapes (steady shapes never reached in flow), and bubble interactions with neighboring bubbles and crystals. The largest source of error in determining shear rate is determination of melt viscosity, which depends on, among other parameters, the water content and temperature of the melt. Both of these parameters must thus be constrained by measurements or petrologic estimates. In contrast, shear stresses are well constrained because the only fluid property required in their calculation is surface tension ($\sigma = \mu G = \Gamma \text{Ca}/a$), which is much less sensitive than viscosity to melt composition and temperature (Murase and McBirney, 1973; Taniguchi, 1988; Walker and Mullin, 1981; Bagdassarov et al., 2000; Mangan and Sisson, 2000). Shear rate and shear stress estimates are more accurate with knowledge of flow type because $D(\text{Ca})$ differs for pure and simple shears. However, misidentifying flow type (pure vs. simple shear) at most contributes an error of a factor of two, and in practice errors from flow type assessments are considerably less. Both bubble relaxation once flow has ceased or slowed, and non-attainment of steady bubble shapes, reduce apparent shear rate and shear stress. Based on analog experiments (Rust and Manga, 2002), if bubbles have relaxed for one characteristic relaxation time
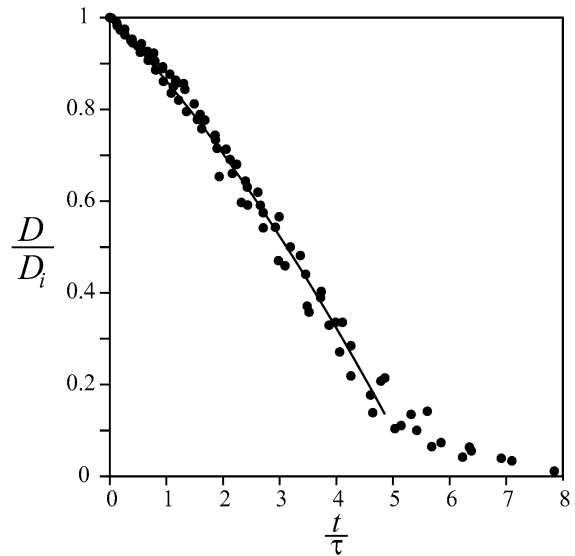

Fig. 13. Experimental results (Rust and Manga, 2002) of shape relaxation of air bubbles in corn syrup ($\mu_s = 118$ Pa s) after simple shear flow has ceased (motor turned off). Data are from four bubbles that began with aspect ratios (l/b) of 9, 18, 20 and 27, with undeformed radii of $a = 0.9$, 2.5, 1.8 and 2.5 mm, respectively. These are the same bubbles as in figure 6 of Rust and Manga (2002). The shape of the bubbles is expressed by D/D_i, where D_i is the deformation parameter $D = (l-b)/(l+b)$ before the motor was turned off and the bubble shape relaxed. Time is non-dimensionalized by dividing by the characteristic relaxation time (Eq. 4). The curve is a second-order polynomial fit to the $t/\tau < 5$ data: $D/D_i = -0.0103(t/\tau)^2 - 0.128(t/\tau) + 1$. Because $D \propto \text{Ca} \propto G$ this relationship is useful to evaluate error due to bubble relaxation in calculation of shear rates from $D(a)$ relationships.

(Eq. 4), the calculated shear rate and shear stress will be about 14% lower than the actual flow parameters (Fig. 13). Because of the high viscosity of rhyolite melt, relaxation times for bubbles in obsidian are long and shape relaxation will generally not be an important factor after fragmentation in explosive eruptions. Bubble interactions on average cause increased bubble deformations (Fig. 14), but numerical simulations of three-dimensional interacting and deforming bubbles in simple shear (Manga and Lowenberg, 2001) indicate that even for $\phi = 0.25$, bubble interactions will result in a less than 10% overestimation of shear rate and shear stress.

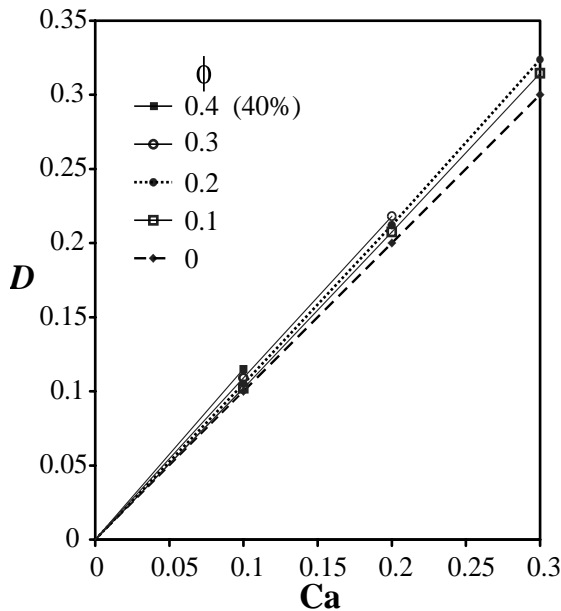Another potential source of error is bubble

Fig. 14. Calculations of bubble deformation (D) for ordered suspensions of three-dimensional bubbles immersed in simple shear flows. Figure 2 of Manga et al. (1998) illustrates the bubble geometries for the calculations. The problem formulation and numerical procedures are the same as those used in Manga and Lowenberg (2001). Values of D are accurate to better than 1%. Numerical simulations for a single bubble suspended in an infinite fluid ($\phi = 0$) agree with small-deformation theory ($D = Ca$). Bubble–bubble interactions lead to greater bubble deformations for a given Ca.

growth during eruption in response to decreasing pressure. Bubble growth rate is controlled by viscous deformation of the surrounding melt. The time scale for bubble growth is $\tau_{growth} = \mu/(\Delta P - 2\Gamma/a)$, where ΔP is the pressure difference between the bubble and surrounding melt (e.g. Navon and Lyakhovsky, 1998; Navon et al., 1998; Stevenson et al., 1997) and $2\Gamma/a$ is the component of this pressure difference due to surface tension. The time scale for deformation of bubbles by shear flow is $\tau_{deformation} = a\mu/\Gamma$ (Hu and Lips, 2001; Rust and Manga, 2002). For a bubble of radius 10 µm and surface tension of 0.3 N/m, $\tau_{deformation} = \tau_{growth}$ for overpressures (ΔP) of order 10^5 Pa. While substantially higher overpressures can be achieved in explosive eruptions (e.g. Navon and Lyakhovsky, 1998; Zhang, 1999), pyro-

clastic obsidian likely forms along conduit walls where ascent velocities are low (Newman et al., 1988; Bursik, 1993). Thus in general we expect ascent rates for effusive and explosive obsidian to be sufficiently slow that the time scale for bubble growth will exceed the time scale for bubbles to deform due to shear flow.

6. Summary and discussion

Surface tension allows steady bubble shapes to be reached in steady shear flow, and thus bubbles record strain rate rather than strain. Flow type (simple vs. pure shear) can be qualitatively assessed from the orientation of bubbles as a function of bubble deformation, as well as from the shape of moderately and highly deformed bubbles (Ca > 1) as a function of Ca. Magma shear rates and shear stresses can be calculated from the deformation of slightly deformed bubbles ($D < 0.5$) for which D and Ca are linearly proportional.

The three case studies presented here demonstrate what information can be determined from bubble geometry analysis (summarized in Table 3). Bubble shapes and orientations indicate that a sample from the spatter-fed MI obsidian flow was deformed by pure shear whereas both a juvenile obsidian clast from the RM pyroclastic fall deposit and an effusive BGM obsidian flow sample were deformed predominantly by simple shear. The RM sample records a higher shear rate and shear stress than the obsidian lava flow samples. The shear rate calculated for the RM pyroclast (0.01 s^{-1}) is three and five orders of magnitude greater than for the MI and BGM samples, respectively. These results are consistent with observations of orders of magnitude decrease in effusion rate between explosive and effusive eruption conditions (Scandone and Malone, 1985; Carey and Sigurdsson, 1989; Nakada et al., 1995; Young et al., 1998). The shear stresses of the BGM sample (22–36 kPa) are of the same order of magnitude as for RM (60 kPa) but the melt viscosity is much greater due to loss of volatiles (0.13 wt% water in BGM vs. 1.1 wt% water in RM), thus resulting in much lower shear rates for BGM. There is no significant shear localiza-

tion in the bands of variable vesicularity in the RM and MI samples, but the component of pure shear in the RM sample is inversely related to layer vesicularity. The BGM obsidian flow sample, which contains bands of variable crystallinity but very low vesicularity ($\phi \ll 0.01$), may, like the RM sample, have deformed by dominantly simple shear with small variations in the component of pure shear in different bands. The BGM data are explained by a small component of pure shear in the higher crystallinity bands and some shape relaxation of all bubbles.

Determining shear rates, shear stresses and flow types from bubbles in obsidian can constrain time scales and physical processes involved in obsidian dome emplacement, conduit flow and the formation of pyroclastic obsidian. Obsidian dome eruptions have never been directly observed. We calculate shear rates of 1.4–2.3×10^{-7} s^{-1} for the Big Glass Mountain obsidian flow sample. These shear rates are at the low end of estimates by Fink (1980) from the spacing of ridges (folds) on this flow (1.4×10^{-4}–8.3×10^{-7} s^{-1}). Castro (1999) calculated a similar shear rate for Obsidian Dome, California based on crystal growth times and total strain indicated by microlite orientation distributions ($G = 7.5 \times 10^{-7}$ s^{-1}). More recently, Castro et al. (2002) estimate a strain rate of 2.3×10^{-8} for Obsidian Dome using an emplacement time based on laboratory experiments (Fink and Griffiths, 1998). For our calculations of BGM strain rates, a strain of one (typical flow front strain (Castro, 1999; Castro et al., 2002)) is reached in 49–80 days.

Flow conditions in volcanic conduits are less well constrained than obsidian lava flow dynamics. Our technique provides estimates of shear rates and stresses near conduit margins, where pyroclastic obsidian probably forms (e.g. Newman et al., 1988; Bursik, 1993). As volatiles may leak into country rocks, information on flow near conduit margins may also provide insights into syn-eruption degassing and the formation of obsidian. There is considerable evidence for open system degassing during transport of magma through volcanic conduits (Newman et al., 1988; Dobson et al., 1989; Taylor, 1991; Jaupart, 1998), but the physical mechanisms by

which exsolved volatiles escape from magma are poorly constrained (Menand and Tait, 2001). Our data from a single Rock Mesa pyroclast show dominantly simple shear deformation. This flow regime will produce permeability anisotropy with the highest permeability parallel to conduit walls and thus favors vertical rather than horizontal gas escape.

In each case study we examined only a single obsidian sample from a lava flow or pyroclastic fall deposit. We do not claim that these samples are representative of the deposits as a whole. In fact, we expect spatial variations in shear type and shear rate in lava flows (e.g. Merle, 1998) and large variations in volatile content (Newman et al., 1988), shear rate, and perhaps flow type within volcanic conduits. In lava flows we anticipate an increasing component of simple shear from top to base and shear localization due to non-homogeneous magma rheology. Although we found only minor shear localization in millimeter-scale banding in our samples, obsidian flows often have meter- and centimeter-scale bands of frothy lava that could be loci for shear localization. Thus, suites of samples with good spatial distribution are required to evaluate flow dynamics in conduits and lava flows.

In this paper we have dealt exclusively with obsidian samples because dilute bubble suspensions are simplest to interpret due to limited bubble–bubble interactions (Fig. 14). While useful information can be gained from analysis of bubbles in obsidian, a similar approach to determining flow parameters from bubbles in pumice would be valuable for understanding conduit processes operative during explosive eruptions. Due to the high bubble content of pumice, bubbles will affect the orientation and shapes of neighboring bubbles by locally disturbing the flow field and through coalescence. Despite complications from these bubble–bubble interactions, there is potential to use the shapes of bubbles in pumice to put limits on the shear rates and shear stresses deforming the magma. Combined with microlite orientation data (e.g. Manga, 1998; Castro et al., 2002), bubble geometry analysis has the potential to provide a complete picture of flow with kinematics from microlites and dynamics from bubbles.

Acknowledgements

References

Acrivos, A., Lo, T.S., 1978. Deformation and breakup of a single slender drop in an extensional flow. J. Fluid Mech. 86, 641–672.

Bagdassarov, N.S., Dingwell, D.B., 1992. A rheological investigation of vesicular rhyolite. J. Volcanol. Geotherm. Res. 50, 307–322.

Bagdassarov, N.S., Dingwell, D.B., Webb, S.L., 1994. Visco-elasticity of crystal- and bubble-bearing rhyolite melts. Phys. Earth Planet. Int. 83, 83–99.

Bagdasarov, N., Dorfman, A., Dingwell, D.B., 2000. Effect of alkalis, phosphorus, and water on the surface tension of haplogranite melt. Am. Min. 85, 33–40.

Bentley, B.J., Leal, L.G., 1986. An experimental investigation of drop deformation and breakup in steady two-dimensional linear flows. J. Fluid Mech. 167, 241–283.

Buckmaster, J.D., 1972. Pointed bubbles in slow viscous flow. J. Fluid Mech. 55, 385–400.

Bursik, M., 1993. Subplinian eruption mechanisms inferred from volatile and clast dispersal data. J. Volcanol. Geotherm. Res. 57, 57–70.

Canedo, E.L., Favelukis, M., Tadmor, Z., Talmon, Y., 1993. An experimental study of bubble deformation in viscous liquids in simple shear flow. Am. Inst. Chem. Eng. J. 39, 553–559.

Carey, S., Sigurdsson, H., 1989. The intensity of plinian eruptions. Bull. Volcanol. 51, 28–40.

Cashman, K.V., 1993. Relationship between plagioclase crystallization and cooling rate in basaltic melts. Contrib. Mineral. Petrol. 113, 126–142.

Castro, J.M., 1999. Textural and structural development of obsidian lavas. Ph.D. Thesis. University of Oregon, 161 pp.

Castro, J.M., Manga, M., Cashman, K.V., 2002. The emplacement of Obsidian Dome, California: Insights from measurements of crystal orientation. Earth Planet. Sci. Lett. 199, 211–226.

Coward, M.P., 1980. The analysis of flow profiles in a basaltic dyke using strained vesicles. J. Geol. Soc. London 137, 605–615.

Cox, R.G., 1969. The deformation of a drop in a general time-dependent fluid flow. J. Fluid Mech. 37, 601–623.

Dobson, P.F., Epstein, S., Stolper, E.M., 1989. Hydrogen isotope fractionation between co-existing vapor and silicate glasses and melts at low pressures. Geochim. Cosmochim. Acta 53, 2723–2730.

Fink, J.H., 1980. Surface folding and viscosity of rhyolite flows. Geology 8, 250–254.

Fink, J.H., Griffiths, R.W., 1998. Morphology, eruption rates, and rheology of lava domes: Insights from laboratory models. J. Geophys. Res. 103, 526–545.

Gardner, J.E., Carey, S., Sigurdsson, H., 1998. Plinian eruptions at Glacier Peak and Newberry volcanoes, United States: Implications for volcanic hazards in the Cascade Range. Geol. Soc. Am. Bull. 110, 173–187.

Grace, H.P., 1971. Dispersion phenomena in high viscosity immiscible fluid systems and application of static mixers as dispersion devices in such systems. Eng. Found. 3rd Conf. Mixing, Andover, NH. Republished in 1982 in Chem. Eng. Commun. 14, 225–277.

Guido, S., Greco, F., 2001. Drop shape under slow steady shear flow and during relaxation. Experimental results and comparison with theory. Rheol. Acta 40, 176–184.

Hammer, J.E., Cashman, K.V., Voight, B., 2000. Magmatic processes revealed by textural and compositional trends in Merapi dome lavas. J. Volcanol. Geotherm. Res. 100, 165–192.

Hess, K.-U., Dingwell, D.B., 1996. Viscosities of hydrous leucogranitic melts: A non-Arrhenian model. Am. Min. 81, 1297–1300.

Hinch, E.J., Acrivos, A., 1980. Long slender drops in a simple shear flow. J. Fluid Mech. 98, 305–328.

Hon, K., Kauahikaua, J., Denlinger, R., Mackay, K., 1994. Emplacement and inflation of pahoehoe sheet flows; observations and measurements of active lava flows on Kilauea Volcano, Hawaii. Geol. Soc. Am. Bull. 106, 351–370.

Hu, Y.T., Lips, A., 2001. Determination of viscosity from drop deformation. J. Rheol. 45, 1453–1463.

Jaupart, C., 1998. Gas loss from magmas through conduit walls during eruption. In: Gilbert, J.S., Sparks, R.S.J. (Eds.), The Physics of Explosive Volcanic Eruptions. Geological Society, London, Spec. Publ. 145, pp. 73–90.

Kennedy, M.R., Pozrikidis, C., Skalak, R., 1994. Motion and deformation of liquid drops, and the rheology of dilute emulsions in shear flow. Comput. Fluids 23, 251–278.

Klug, C., Cashman, K.V., 1996. Permeability development in vesiculating magma. Bull. Volcanol. 58, 87–100.

Klug, C., Cashman, K.V., Bacon, C.R., 2002. Structure and physical characteristics of pumice from the climactic eruption of Mt. Mazama (Crater Lake). Oregon. Bull. Volcanol. 64, 486–501.

Kouchi, A., Tsuchiyama, A., Sunagawa, I., 1986. Effect of stirring on crystallization kinetics of basalt: texture and element partitioning. Contrib. Mineral. Petrol. 93, 429–438.

Lejeune, A., Richet, P., 1995. Rheology of crystal-bearing silicate melts; an experimental study at high viscosities. J. Geophys. Res. B 100, 4215–4229.

Loewenberg, M., Hinch, E.J., 1996. Numerical simulation of concentrated emulsion in shear flow. J. Fluid Mech. 321, 395–419.

Manga, M., 1998. Orientation distribution of microlites in obsidian. J. Volcanol. Geotherm. Res. 86, 107–115.

Manga, M., Castro, J., Cashman, K.V., Loewenberg, M.,

1998. Rheology of bubble-bearing magmas. J. Volcanol. Geotherm. Res. 87, 15–28.

Manga, M., Lowenberg, M., 2001. Viscosity of magmas containing highly deformable bubbles. J. Volcanol. Geotherm. Res. 105, 19–24.

Mangan, M., Sisson, T.W., 2000. Delayed, disequilibrium degassing in rhyolite magma; decompression experiments and implications for explosive volcanism. Earth Planet. Sci. Lett. 183, 441–455.

Menand, T., Tait, S.R., 2001. A phenomenological model for precursor volcanic eruptions. Nature 411, 678–680.

Merle, O., 1998. Internal strain within lava flows from analogue modelling. J. Volcanol. Geotherm. Res. 81, 189–206.

Murase, T., McBirney, A.R., 1973. Properties of some common igneous rocks and their melts at high temperature. Geol. Soc. Am. Bull. 84, 3563–3592.

Nakada, S., Miyake, Y., Sato, H., Oshima, O., Fujinawa, A., 1995. Endogenous growth of dacite dome at Unzen Volcano (Japan), 1993-1994. Geology 23, 157–160.

Navon, O., Lyakhovsky, V., 1998. Vesiculation processes in silicic magmas. In: Gilbert, J.S., Sparks, R.S.J. (Eds.) The Physics of Explosive Volcanic Eruptions. Geol. Soc. Lond. Spec. Publ. 145, pp. 27–50.

Navon, O., Chekhmir, A., Lyakhovsky, V., 1998. Bubble growth in highly viscous melts; theory, experiments, and autoexplosivity of dome lavas. Earth Planet. Sci. Lett. 160, 763–776.

Newman, S., Epstein, S., Stolper, E.M., 1988. Water, carbon dioxide and hydrogen isotopes in glasses from the ca 1340, A.D. eruption of the Mono Craters, California: constraints on degassing phenomena and initial volatile content. J. Volcanol. Geotherm. Res. 35, 75–96.

Pinkerton, H., Norton, G.E., 1995. Rheological properties of basaltic lavas at sub-liquidus temperature: laboratory and field measurements on lavas from Mount Etna. J. Volcanol. Geotherm. Res. 68, 307–323.

Polacci, M., Papale, P., 1997. The evolution of lava flows from ephemeral vents at Mount Etna: insights from vesicle distribution and morphological studies. J. Volcanol. Geotherm. Res. 76, 1–17.

Pozrikidis, C.J., 1993. On the transient motion of ordered suspensions of liquid drops. J. Fluid Mech. 246, 301–320.

Rallison, J.M, 1980. Note on the time-dependent deformation of a viscous drop which is almost spherical. J. Fluid Mech. 98, 625–633.

Rallison, J.M., 1981. A numerical study of the deformation and burst of a viscous drop in general shear flows. J. Fluid Mech. 109, 465–482.

Rallison, J.M., 1984. The deformation of small viscous drops and bubbles in shear flows. Annu. Rev. Fluid Mech. 16, 45–66.

Rodgers, J.P., 1996. Analysis of tephra components from Rock Mesa, South Sister Volcano, Oregon: Implications for evolution of the explosive phase. M.Sc. Thesis. University of Oregon, 85 pp.

Rust, A.C., Manga, M., 2002. Bubble shapes and orientations in low Re simple shear flow. J. Colloid Interface Sci. 249, 476–480.

Ryerson, F.J., Weed, H.C., Piwinskii, A.J., 1988. Rheology of subliquidus magmas; 1, Picritic compositions. J. Geophys. Res. B 93, 3421–3436.

Scandone, R., Malone, S.D., 1985. Magma supply, magma discharge and readjustment of the feeding system of Mount St. Helens during 1980. J. Volcanol. Geotherm. Res. 23, 239–262.

Schulze, F., Behrens, H., Holtz, F., Roux, J., Johannes, W., 1996. The influence of H_2O on the viscosity of a haplogranitic melt. Am. Mineral. 81, 1155–1165.

Scott, W.E., 1987. Holocene rhyodacite eruptions on the flanks of South Sister volcano, Oregon. Geol. Soc. Am. Spec. Paper 212, 35–53.

Self, S., Keszthelyi, L., Thordarson, T., 1998. The importance of pahoehoe. Annu. Rev. Earth Planet. Sci. 26, 81–110.

Shelley, D., 1985. Determining paleo-flow directions from groundmass fabrics in the Lyttleton radial dykes, New Zealand. J. Volcanol. Geotherm. Res. 25, 69–79.

Smith, J.V., 2000. Textural evidence for dilatant (shear thickening) rheology of magma at high crystal concentrations. J. Volcanol. Geotherm. Res. 99, 1–7.

Stevenson, R.J., Briggs, R.M., Hodder, P.W., 1993. Emplacement history of a low-viscosity, fountain-fed pantelleritic lava flow. J. Volcanol. Geotherm. Res. 57, 39–56.

Stevenson, R.J., Dingwell, D.B., Webb, S.L., Bagdassarov, N.S., 1995. The equivalence of enthalpy and shear stress relaxation in rhyolitic obsidians and quantification of the liquid-glass transition in volcanic processes. J. Volcanol. Geotherm. Res. 68, 297–306.

Stevenson, R.J., Bagdassarov, N.S., Romano, C., 1997. Vesiculation processes in a water-rich calc-alkaline obsidian. Earth Planet. Sci. Lett. 146, 555–571.

Stone, H.A., 1994. Dynamics of drop deformation and breakup in viscous fluids. Annu. Rev. Fluid Mech. 26, 65–102.

Taniguchi, H., 1988. Surface tension of melts in the system $CaMgSi_2O_6$-$CaAl_2Si_2O_8$ and its structural significance. Contrib. Mineral. Petrol. 100, 484–489.

Taylor, B.E., 1991. Degassing of Obsidian Dome rhyolite, Inyo volcanic chain, California. In: Taylor, H.P., Jr., O'Neil, J.R., Kaplan, I.R. (Eds.), Stable Isotope Geochemistry: A Tribute to Samuel Epstein. Geochem. Soc. Spec. Publ. 3, pp. 339–353.

Taylor, G.I., 1932. The viscosity of a fluid containing small drops of another fluid. Proc. R. Soc. London A 138, 41–48.

Taylor, G.I., 1934. The formation of emulsions in definable fields of flow. Proc. R. Soc. London A 146, 501–523.

Tobisch, O.T., Williams, Q., 1998. Use of microgranitoid enclaves as solid state strain markers in deformed granitic rock: an evaluation. J. Structural Geol. 20, 727–743.

Toramaru, A., 1988. Formation of propagation pattern in two-phase flow systems with application to volcanic eruptions. Geophys. J. Royal Astr. Soc. 95, 613–623.

Toramaru, A., 1989. Vesiculation process and bubble size distribution in ascending magmas with constant velocities. J. Geophys. Res. 94, 17523–17542.

Torza, S., Cox, R.G., Mason, S.G., 1972. Paricle motions in sheared suspension. XXVII. Transient and steady deformation and burst of liquid drops. J. Colloid Interface Sci. 38, 395–411.

Uijttewaal, W.S.J., Nijhof, E., 1995. The motion of a droplet subjected to linear shear flow including the presence of a plane wall. J. Fluid Mech. 302, 45–63.

Ventura, G., 2001. The strain path and emplacement mechanism of lava flows; an example from Salina (southern Tyrrhenian Sea, Italy). Earth Planet. Sci. Lett. 188, 229–240.

Vernon, R.H., 1987. A microstructural indicator of shear sense in volcanic rocks and its relationship to porphyroblast rotation in metamorphic rocks. J. Geol. 95, 127–133.

Walker, D., Mullin, O., Jr., 1981. Surface tension of natural silicate melts from 1200-1500°C and implications for melt structure. Contrib. Mineral. Petrol. 76, 455–462.

Webb, S.L., Dingwell, D.B., 1990. Non-Newtonian rheology of igneous melts at high stresses and strain rates; experimental results for rhyolite, andesite, basalt, and nephelinite. J. Geophys. Res. B 95, 15695–15701.

Williams, Q., Tobisch, O.T., 1994. Microgranitic enclave shapes and magmatic strain histories: Constraints from drop deformation theory. J. Geophys. Res. 99, 24359–24368.

Young, S.R., Sparks, R.S.J., Aspinall, W.P., Lynch, L.L., Miller, A.D., Robertson, R.E.A., Shepherd, J.B., 1998. Overview of the eruption of Soufriere Hills Volcano, Montserrat, 18 July 1995 to December 1997. Geophys. Res. Lett. 25, 3389–3392.

Zhang, Y., 1999. A criterion for the fragmentation of bubbly magma based on brittle failure theory. Nature 402, 648–650.

Zhang, Y., Xu, A., Behrens, H., 2000. Hydrous species geospeedometer in rhyolite; improved calibration and application. Geochim. Cosmochim. Acta 64, 3347–3355.